Computer Programs in Physics

BIMBAMBUM: A potential flow solver for single cavitation bubble dynamics ☆,☆☆

Armand Baptiste Sieber [a],*, Henri Hugo Sieber [b], Davide Bernardo Preso [a], Mohamed Farhat [a]

[a] Institute of Mechanical Engineering, École Polytechnique Fédérale de Lausanne, 1007 Lausanne, Switzerland
[b] Institute for Particle Physics and Astrophysics, ETH Zürich, 8093 Zürich, Switzerland

ARTICLE INFO

ABSTRACT

In the absence of analytical solutions for the dynamics of non-spherical cavitation bubbles, we have implemented a numerical simulation solver based on the boundary integral method (BIM) that models the behavior of a single bubble near an interface between two fluids. The density ratio between the two media can be adjusted to represent different types of boundaries, such as a rigid boundary or a free surface. The solver allows not only the computation of the dynamics of the bubble and the fluid-fluid interface, but also, in a secondary processing phase, the computation of the surrounding flow field quantities. We present here the detailed implementation of this solver and validate its capabilities using theoretical solutions, experimental observations, and results from other simulation softwares. This solver is called BIMBAMBUM which stands for **B**oundary **I**ntegral **M**ethod for **B**ubble **A**nalysis and **M**odeling in **B**ounded and **U**nbounded **M**edia.

Program summary
Program Title: BIMBAMBUM
CPC Library link to program files: https://doi.org/10.17632/89vv35pmhr.1
Licensing provisions: GPLv3
Programming language: C++ and Python
Nature of problem: The code solves the axisymmetric dynamics of single cavitation bubble in the vicinity of different types of boundaries. The boundaries are treated as an interface between two fluids, where the fluids can have different density ratios. The two fluids are considered inviscid and incompressible and the associated flows irrotational so that Laplace's equation is valid everywhere.
Solution method: A boundary integral method is used to calculate the velocities on the discretized bubble surface and the fluid-fluid interface. The position of these boundaries can then be updated in time using a Lagrangian approach. In the fluid domain surrounding the bubble, the velocities and pressure are estimated using a combination of the boundary integral method and finite differences.
Additional comments including restrictions and unusual features: The code solves the bubble dynamics as long as its surface remains simply connected.

1. Introduction

Cavitation refers to the formation of vapor and gas-filled cavities in a liquid following a sudden drop in pressure. These cavities, known as cavitation bubbles, are a subject of significant and growing interest owing to the many processes in which they are found. Traditionally observed around ship propellers and hydraulic turbines, where they cause

unwanted and deteriorating effects [1,2], cavitation bubbles are now gradually being used in biomedical, chemical and cleaning applications, with the aim of exploiting their powerful properties [3–5].

Due to the diversity and nature of these applications, an accurate understanding of the behavior of the bubbles is critical for the safe and efficient use of cavitation. For that purpose, the study of the bubbles fundamental dynamics is often reduced to a simplified test case: the
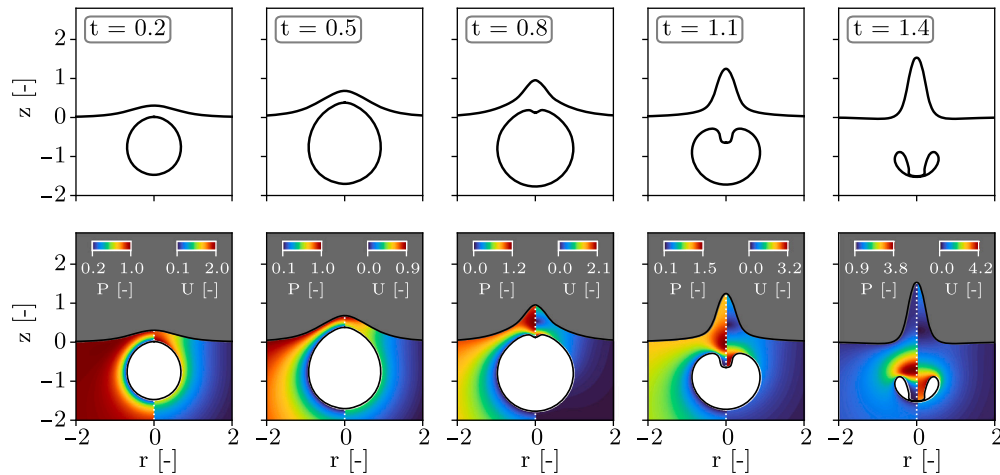
Fig. 1. Growth and collapse of a bubble near a free-surface at $\gamma = 0.8$. The first row demonstrates the results obtained with the first processing stage only. The second row shows the associated pressure (left halves of the frames) and velocity (right halves of the frames) fields obtained with the second processing stage. All units are dimensionless.

growth and collapse of a single bubble. If the bubble remains spherical throughout its lifetime, there are a number of 1D theoretical models that can be used to study the dynamics of the bubble oscillation [6–11]. However, when the bubble exhibits an aspherical behavior, as it is the case for oscillations near a boundary, other approaches are generally required to study the dynamics of the bubble and the deformation of its surface. One of these approaches is numerical simulations which allow the modeling of a wide range of flow configurations and provide valuable information about the nature of the flow field surrounding the bubble. In that case, the governing Navier-Stokes or Euler equations may be solved with grid-based methods that employ level-set [12–14], front-tracking [15–17], volume of fluid [18–20] or diffuse-interface [21–23] techniques to capture the interface between the bubble and the liquid. These methods provide accurate results that compare well with experiments, but they can be computationally expensive as the number of cells required to solve the problem in an axisymmetric configuration is generally of the order of $\mathcal{O}(10^5)$ cells. Alternatively, if one assumes the flow incompressible and potential during the lifetime of the bubble, Laplace's equation is satisfied and the boundary integral method (BIM) may be used. The BIM makes it possible to find the velocity potential anywhere in the numerical domain by solely solving the flow problem at the edges of the domain. This means that only the boundaries of the numerical domain need to be meshed, thus significantly reducing the computational cost. Initiated by Blake and collaborators to model the growth and collapse of bubbles near flat rigid walls and free surfaces [24–26], the use of BIM has since been widely adopted to study the behavior of single cavitation bubble in a variety of configuration, such as near planar or curved rigid interfaces, free-surfaces, elastic interfaces, fluid-fluid interfaces or even in tubular vessels [27–38]. Compared to grid-based methods, the BIM can significantly reduce the computational cost of a simulation, as demonstrated by Li et al. [29] for a bubble collapsing near a rigid surface. The authors reported a 16-minute computation time for a BIM simulation running on a single core of a personal desktop, as opposed to 13000 core-hours needed to run a volume of fluid simulation of the same bubble.

Many of the references cited above have contributed to the improvement of the BIM with the objective of better understanding and predicting the behavior of cavitation bubbles. Nevertheless, the numerical solvers these references describe have essentially been developed in-house by the different research teams and are rarely open access. Although open-source Boundary Integral/Element Method packages such as Bempp [39], Bembel [40] or BESLE [41] exist, they are not specifically designed for single cavitation bubble dynamics simulations. We have developed such solver that we successfully employed to describe the dynamics of cavitation bubbles near granular boundaries, which we

modeled as equivalent liquid [42], near elastic interfaces [43] or near a rigid boundary [44]. We now wish to make this solver publicly available with the vocation to allow research teams, students and any other interested person to quickly get insights into the behavior of cavitation bubbles and hopefully to provide a basis for an accelerated and collaborative developments of this solver.

In this work we thus present the version 1.0 of BIMBAMBUM, which stands for **B**oundary **I**ntegral **M**ethod for **B**ubble **A**nalysis and **M**odeling in **B**ounded and **U**nbounded **M**edia. The solver models the dynamics of single cavitation bubbles, assuming axial symmetry in the bubble shape and flow field, and allows these dynamics to be considered in a variety of flow configurations. In section 2 we provide a short overview of the solver structure and introduce its dependencies. Section 3 describes the equations governing the flow field and section 4 the numerical implementation of these equations. We finally validate the code in section 5.

2. Solver overview and dependencies

BIMBAMBUM is a two-stage potential flow solver designed to model the dynamics of a cavitation bubble near an initially flat boundary. The first stage, also referred to as main stage, computes the time evolution of the surfaces of the bubble and nearby boundary. The second stage computes the velocity and pressure fields associated with the bubble dynamics at any selected time point in the bubble lifetime. Both stages of the solver must be executed separately. The first processing stage can be used as stand-alone if the user only wants to calculate the dynamics of the bubble. The secondary processing stage, on the other hand, requires the results of the first stage as inputs. Sample results obtained with the first and second processing stage are illustrated in Fig. 1 for a bubble evolving near a free surface.

BIMBAMBUM is largely written in C++ to allow fast computation of bubble dynamics on a personal computer. The main processing stage is fully written in C++ and employs the modular nature of the language through polymorphism and inheritence of classes allowing for facilitated further developments. The solver relies on the Armadillo library for linear algebra [45,46] and on the GNU scientific library [47] for numerical integrations. To accelerate the computation, the performance-critical tasks are moreover parallelized using the multi-processing library OpenMP [48]. Finally, the BOOST library is used to parse the JSON input data in C++ [49]. The secondary processing stage is partially written in Python and relies on the following freely available open source libraries: Numpy [50] and Matplotlib [51]. Yet, the performance critical tasks are written in C++ and integrated into the Python program as an extension module using pybind11 [52].
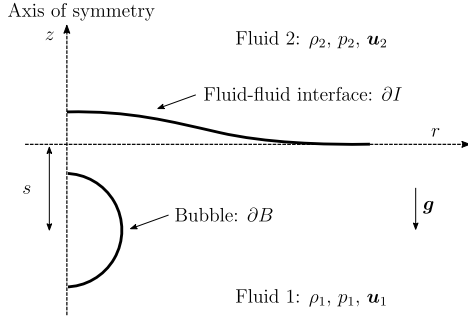
Fig. 2. Computational domain.

3. Mathematical model

3.1. Physical domain and governing equations

We consider the growth and collapse of a single cavitation bubble in a liquid of density ρ_1. Since most of the phenomena associated with single bubble dynamics may be seen as axisymmetric, we treat this problem in a 2D configuration with coordinates (r, z), as illustrated in Fig. 2. The domain occupied by fluid 1 is denoted as D_1 and is delimited by a boundary ∂D_1 consisting of the bubble surface, ∂B, and an infinite interface ∂I. On the other side of this interface we consider a second fluid of density ρ_2 and domain D_2, delimited by the boundary ∂D_2 which solely consists of ∂I. Both fluids are subjected to gravity $\boldsymbol{g}$. Considering a fluid-fluid interface with a density jump provides a generalization of the already well-documented interactions of cavitation bubbles with rigid boundaries and free surfaces [27,28,32,33], where a density ratio $\rho_1/\rho_2 \to 0$ models the behavior of a bubble near a rigid wall, $\rho_1/\rho_2 \to \infty$ near a free surface and $\rho_1/\rho_2 = 1$ simulates a bubble in an unbounded liquid, as shown by Klaseboer and Khoo [34]. In agreement the majority of other works in the literature [27,28,32,33], the two fluids under consideration are assumed inviscid and incompressible and the associated flows irrotational. These assumptions are acceptable given that most of the bubble dynamics are inertia dominated and viscous effects are concentrated in thin boundary layers near the surfaces. It should nonetheless be emphasized that compressibility effects of the liquid can be important in the final instants of the bubble collapse, where its interface velocity may become significant with respect to the liquid speed of sound. The above assumptions lead to the velocity being expressed as the gradient of a potential $\boldsymbol{u_i} = \nabla \phi_i$, with $i = 1, 2$. In that case, the following equations are valid in both fluids [34,53],

$$\nabla^2 \phi_i = 0 \tag{1}$$

$$\frac{\partial \phi_i}{\partial t} + \frac{|\nabla \phi_i|^2}{2} + \frac{p_i}{\rho_i} + g(z_i - z_0) = \frac{p_\infty}{\rho_i} \tag{2}$$

Equation (1) is Laplace's equation and equation (2) is the Bernoulli equation, where p_∞ is the far-field reference pressure and z_0 is a reference coordinate of the system at rest. The bubble, which would reach a maximum radius R_m in an unbounded medium, is initially located at a distance s from the interface. We consider that it is uniformly filled with a combination of liquid vapor with constant pressure, p_v, and non-condensable gas with pressure p_g. The heat and mass transfer across the interface are neglected and the gas is considered as ideal yielding an adiabatic process with a gas pressure given by $p_g = p_{g,0}(V_0/V)^k$, where $p_{g,0}$ and V_0 are the initial gas pressure and bubble volume, respectively, and V is the instantaneous bubble volume. The superscript k denotes the ratio of specific heat. Hence, we can write the pressure within the bubble as [54],

$$p_b = p_v + p_{g,0}(V_0/V)^k \tag{3}$$

The case of zero non-condensable gas content may also be considered in the simulation and would result in a bubble solely filled with liquid vapor.

At the liquid-liquid interface, we include the possibility to mimic the effects of an elastic boundary. This is done by considering an interfacial tension between the two immiscible fluids [35,55]. As a result, the pressure directly above and directly below the interface is related by the Young-Laplace equation,

$$p_1 = p_2 + \sigma K \tag{4}$$

where σ is the interfacial tension and K represents the curvature of the interface.

3.2. Non-dimensionalization

For the sake of convenience, we scale all terms and solely consider dimensionless quantities. To that end, we follow the work of Blake et al. [25,26] and scale the lengths by the bubble maximum radius R_m, the time by $R_m \sqrt{\rho_1/\Delta p}$ and the pressure p by $(p - p_v)/\Delta p$, where $\Delta p = p_\infty - p_v$. This yields the following set of dimensionless quantities,

$$\gamma = \frac{s}{R_m} \qquad \epsilon = \frac{p_{g,0}}{\Delta p} \qquad \delta = \frac{\rho_1 g R_m}{\Delta p} \qquad \bar{\sigma} = \frac{\sigma}{R_m \Delta p} \tag{5}$$

where γ is the stand-off distance, ϵ is the strength parameter, δ is the buoyancy parameter and $\bar{\sigma}$ represents the dimensionless surface tension. The notation $\alpha = \rho_1/\rho_2$ is additionally used to represent the density ratio. We note here that for small bubbles, $R_m \sim \mathcal{O}(10^{-3}\ \text{m})$, the effects of gravity scale as $\delta \sim \mathcal{O}(10^{-4})$ in water at atmospheric condition and may be neglected.

3.3. Dynamic and kinematic boundary conditions

Since the BIM formulation requires the values of the potentials on the boundaries of the fluid domain, an appropriate set of boundary conditions must be employed on ∂B and ∂I. At the bubble interface, the dynamics boundary condition requires that the pressure within the bubble and in the flow be equated. This is achieved by combining equations (2) and (3), where the value of z_0 is taken as the initial position of the bubble, γ, assuming that all points on its surface originate from a single location. Neglecting surface tension, this yields in dimensionless form,

$$\frac{\partial \phi_1}{\partial t} + \frac{|\nabla \phi_1|^2}{2} + \epsilon \left(\frac{V_0}{V}\right)^k + \delta(z - \gamma) - 1 = 0 \tag{6}$$

At the liquid-fluid interface, the formation of holes between the two liquid phases is avoided by ensuring that the normal velocities are continuous across the interface. Given that we include an interfacial tension to mimic elastic effects, the pressure directly above and directly below the interface is related by the Young-Laplace equation, so that the dimensionless dynamic boundary condition is given by,

$$\frac{\partial(\phi_2 - \alpha \phi_1)}{\partial t} + \frac{|\nabla \phi_2|^2 - \alpha|\nabla \phi_1|^2}{2} + \delta(1 - \alpha)z - \alpha \bar{\sigma} \bar{K} = 0 \tag{7}$$

Note that the value $z_0 = 0$ is considered at the fluid-fluid interface. Following the formulation of Klaseboer and Khoo [34,36], all surfaces are treated in a Lagrangian manner where the material derivatives D/Dt are taken with respect to fluid 1 so that $Dx/Dt = \partial x/\partial t + \nabla \phi_1 \cdot \nabla x$. The rate of change of the potential thus takes the following form on the boundaries of the bubble ∂B,

$$\frac{D\phi_1}{Dt} = \frac{|\nabla \phi_1|^2}{2} + 1 - \epsilon \left(\frac{V_0}{V}\right)^k - \delta(z - \gamma) \tag{8}$$

and at the fluid-fluid interface ∂I,

$$\frac{DF}{Dt} = \left(\nabla \phi_1 \cdot \nabla \phi_2 - \frac{|\nabla \phi_2|^2}{2} - \alpha \frac{|\nabla \phi_1|^2}{2}\right) - \delta(1 - \alpha)z + \alpha \bar{\sigma} \bar{K} \tag{9}$$

where $F = \phi_2 - \alpha\phi_1$. Finally, the position of the bubble surface and the fluid-fluid interface is subjected to the following kinematic condition,

$$\frac{D\boldsymbol{x}}{Dt} = \nabla\phi_1 \tag{10}$$

where $\boldsymbol{x} = (r, z)$ is a point on the boundaries of the domain and $\nabla\phi_1 = (\partial\phi_1/\partial n, \partial\phi_1/\partial s)$, with $\partial\phi_1/\partial n$ the normal and $\partial\phi_1/\partial s$ the tangential velocity on the boundaries of fluid 1.

4. Numerical implementation

4.1. Boundary integral method

The solution to equation (1) may be found by solving a boundary integral equation, where the potential in the fluid domain can be derived as a function of the potential and its normal derivative on the boundaries of the domain. It follows that the solution at a point $\boldsymbol{y}$ inside the fluid domains can be found by solving the following direct boundary integral in fluid 1 with domain D_1,

$$c_1(\boldsymbol{y})\phi_1(\boldsymbol{y}) + \int_{\boldsymbol{x}\in\partial D_1} \phi_1(\boldsymbol{x})\frac{\partial G(\boldsymbol{y},\boldsymbol{x})}{\partial n}\mathrm{d}s = \int_{\boldsymbol{x}\in\partial D_1} G(\boldsymbol{y},\boldsymbol{x})\frac{\partial\phi_1(\boldsymbol{x})}{\partial n}\mathrm{d}s \tag{11}$$

and in fluid 2 with domain D_2,

$$c_2(\boldsymbol{y})\phi_2(\boldsymbol{y}) - \int_{\boldsymbol{x}\in\partial D_2} \phi_2(\boldsymbol{x})\frac{\partial G(\boldsymbol{y},\boldsymbol{x})}{\partial n}\mathrm{d}s = \int_{\boldsymbol{x}\in\partial D_2} G(\boldsymbol{y},\boldsymbol{x})\frac{\partial\phi_2(\boldsymbol{x})}{\partial n}\mathrm{d}s \tag{12}$$

where $G(\boldsymbol{y},\boldsymbol{x}) = 1/|\boldsymbol{y} - \boldsymbol{x}|$ is the Green function. The coefficients c_1 and c_2 are the solid angles which, for smooth boundaries, satisfy,

$$c_{1,2}(\boldsymbol{y}) = \begin{cases} 2\pi & \text{if } \boldsymbol{y}\in\partial D_{1,2}, \\ 4\pi & \text{if } \boldsymbol{y}\in D_{1,2}\setminus\partial D_{1,2} \end{cases} \tag{13}$$

Since only the boundaries of the domain need to be meshed to solve the integrals in equations (11) and (12), the use of the boundary integral method makes it possible to reduce the originally two-dimensional axisymmetric problem to a one-dimensional problem.

4.2. Discretization and integration

The integrals in equations (11) and (12) are computed using a collocation method where the surfaces of the bubbles and the fluid-fluid interface are discretized in N_b and N_s elements, respectively, resulting in $N_\mathrm{b} + 1$ and $N_\mathrm{s} + 1$ node points. The bubble and fluid-fluid interface surfaces are represented by cubic splines fitted through the node points and parametrized with respect to the surfaces arc length ξ. At the nodes, the potentials take the value ϕ_j and their normal derivatives the value $\psi_j = \partial\phi_j/\partial n$. Both quantities are assumed to vary linearly between two adjacent node points. With these considerations, equation (11) may be discretized as follows (a similar discretization applies to equation (12)),

$$c_{\mathrm{p},i}\phi_i + A_{i,j}\phi_j = B_{i,j}\psi_j \tag{14}$$

where ϕ_i is the potential at $\boldsymbol{y} = (r_i, z_i)$. The coefficient matrix $\boldsymbol{A}$ contains the discretized integral of the normal derivative of the Green's function and the matrix $\boldsymbol{B}$ contains the discretized integral of the Green's function. Both matrices additionally take into account the linear interpolation between the nodal points. These quantities, the detailed derivation of which can be found in the work of Taib [24] or Curtiss [53], have the following forms in axisymmetric coordinates,

$$A_{i,j} = -\int_{\xi_{j-1}}^{\xi_j} \left(\frac{\xi - \xi_{j-1}}{\xi_j - \xi_{j-1}}\right) \frac{4r(\xi)}{\left((r(\xi) + r_i)^2 + (z(\xi) - z_i)^2\right)^{1.5}} \left(\frac{2z'(\xi)r_i K(k(\xi))}{k(\xi)^2}\right.$$
$$+ \left[z'(\xi)(r(\xi) + r_i) - r'(\xi)(z(\xi) - z_i) - \frac{2z'(\xi)r_i}{k(\xi)^2}\right]\left.\frac{E(k(\xi))}{1 - k(\xi)^2}\right)\mathrm{d}\xi$$

$$-\int_{\xi_j}^{\xi_{j+1}} \left(\frac{\xi_{j+1} - \xi}{\xi_{j+1} - \xi_j}\right) \frac{4r(\xi)}{\left((r(\xi) + r_i)^2 + (z(\xi) - z_i)^2\right)^{1.5}} \left(\frac{2z'(\xi)r_i K(k(\xi))}{k(\xi)^2}\right.$$
$$+ \left[z'(\xi)(r(\xi) + r_i) - r'(\xi)(z(\xi) - z_i) - \frac{2z'(\xi)r_i}{k(\xi)^2}\right]\left.\frac{E(k(\xi))}{1 - k(\xi)^2}\right)\mathrm{d}\xi \tag{15}$$

and,

$$B_{i,j} = \int_{\xi_{j-1}}^{\xi_j} \left(\frac{\xi - \xi_{j-1}}{\xi_j - \xi_{j-1}}\right) \frac{4r(\xi)\sqrt{r'(\xi)^2 + z'(\xi)^2}K(k(\xi))}{\sqrt{(r(\xi) + r_i)^2 + (z(\xi) - z_i)^2}}\mathrm{d}\xi$$

$$+ \int_{\xi_j}^{\xi_{j+1}} \left(\frac{\xi_{j+1} - \xi}{\xi_{j+1} - \xi_j}\right) \frac{4r(\xi)\sqrt{r'(\xi)^2 + z'(\xi)^2}K(k(\xi))}{\sqrt{(r(\xi) + r_i)^2 + (z(\xi) - z_i)^2}}\mathrm{d}\xi \tag{16}$$

with,

$$k^2(\xi) = \frac{4r(\xi)r_i}{(r(\xi) + r_i)^2 + (z(\xi) - z_i)^2} \tag{17}$$

The functions $K(k)$ and $E(k)$ are the complete elliptic integrals of the first and second kind, respectively, and their values are estimated with 12th order polynomial approximation as in Pearson [56],

$$K(k) \approx P(1 - k^2) - Q(1 - k^2)\log(1 - k^2) \tag{18}$$

$$E(k) \approx R(1 - k^2) - S(1 - k^2)\log(1 - k^2) \tag{19}$$

where P, Q, R and S are the tabulated polynomials, the coefficients of which are provided in Appendix A. Note that the polynomials used in this work slightly differ from the ones employed by Pearson [56].

Singularities occur when evaluating the boundary integrals if $\boldsymbol{x} = (r(\xi), z(\xi))$ approaches $\boldsymbol{y} = (r_i, z_i)$, since the value of the Green function ($G(\boldsymbol{y},\boldsymbol{x}) = 1/|\boldsymbol{y} - \boldsymbol{x}|$) and its normal derivative tend towards infinity. In the axisymmetric configuration considered in this work, these singularities appear as weak logarithmic singularities in the evaluation the complete elliptic integrals when $1 - k^2$ approaches zero. We therefore integrate equations (15) and (16) using the *QAGS* routine provided in the GNU scientific library [47]. This routine performs a 21-points Gauss-Konrod quadrature on adaptively refined subintervals concentrating the new subinterval around possible singularities. It is however worth noting that there exist non-singular formulations of the boundary integral method that allow the use of standard quadrature methods to estimate the surface integrals [57,58].

4.3. Determination of normal and tangential velocities at the boundaries

The normal velocities at the domain boundaries are determined by evaluating the potentials ϕ_i at the node points with discrete coordinates $r_i = r(\xi_i)$ and $z_i = z(\xi_i)$. In this case, equation (11) can be rewritten into the following system of $N_b + N_s + 2$ linear equations,

$$\begin{bmatrix} 2\pi\boldsymbol{I}_\mathrm{b} + \boldsymbol{A}_1 & \boldsymbol{A}_2 \\ \boldsymbol{A}_3 & 2\pi\boldsymbol{I}_\mathrm{s} + \boldsymbol{A}_4 \end{bmatrix} \begin{bmatrix} \boldsymbol{\phi}_{1,\mathrm{b}} \\ \boldsymbol{\phi}_{1,\mathrm{s}} \end{bmatrix} = \begin{bmatrix} \boldsymbol{B}_1 & \boldsymbol{B}_2 \\ \boldsymbol{B}_3 & \boldsymbol{B}_4 \end{bmatrix} \begin{bmatrix} \boldsymbol{\psi}_{1,\mathrm{b}} \\ \boldsymbol{\psi}_{1,\mathrm{s}} \end{bmatrix} \tag{20}$$

and equation (12) into the following $N_s + 1$ system,

$$\left[2\pi\boldsymbol{I}_\mathrm{s} - \boldsymbol{A}_4\right]\boldsymbol{\phi}_{2,\mathrm{s}} = \boldsymbol{B}_4\boldsymbol{\psi}_{2,\mathrm{s}} \tag{21}$$

where $\boldsymbol{A}_{1\text{-}4}$ are sub-matrices of $\boldsymbol{A}$ and $\boldsymbol{B}_{1\text{-}4}$ are submatrices of $\boldsymbol{B}$. The subscript 1 indicates contributions to the boundary integrals where $\boldsymbol{y}\in\partial B$ and $\boldsymbol{x}\in\partial B$, the subscript 2 where $\boldsymbol{y}\in\partial I$ and $\boldsymbol{x}\in\partial B$, the subscript 3 where $\boldsymbol{y}\in\partial B$ and $\boldsymbol{x}\in\partial I$ and the subscript 4 where $\boldsymbol{y}\in\partial I$ and $\boldsymbol{x}\in\partial I$. The subscript b refer to quantities on the bubble surface and the subscript s to quantities on the fluid-fluid interface. $\boldsymbol{I}_\mathrm{b}$ is the ($N_\mathrm{b} + 1 \times N_\mathrm{b} + 1$) identity matrix, and $\boldsymbol{I}_\mathrm{s}$ the ($N_\mathrm{s} + 1 \times N_\mathrm{s} + 1$) identity matrix.

We then use the formulation introduced by Klaseboer and Khoo [34, 36] to rewrite equations (20) and (21) in a set of two coupled blocks

and one independent block of linear equations that take into account the relationship between the potentials on both sides of the interface. A detailed description of this implementation is provided in the work of the authors, so we only give the final results of their derivation,

$$
\begin{bmatrix} -\boldsymbol{B_1} & \boldsymbol{A_2}(1-\alpha) \\ -\boldsymbol{B_3} & 2\pi\boldsymbol{I} + \boldsymbol{A_4} + \alpha(2\pi\boldsymbol{I} - \boldsymbol{A_4}) \end{bmatrix} \begin{bmatrix} \boldsymbol{\psi}_{1,\mathrm{b}} \\ \boldsymbol{\phi}_{1,\mathrm{s}} \end{bmatrix}
$$
$$
= \begin{bmatrix} -(2\pi\boldsymbol{I} + \boldsymbol{A_1})\boldsymbol{\phi}_{1,\mathrm{b}} + \boldsymbol{A_2}\boldsymbol{F} \\ -\boldsymbol{A_3}\boldsymbol{\phi}_{1,\mathrm{b}} - (2\pi\boldsymbol{I} - \boldsymbol{A_4})\boldsymbol{F} \end{bmatrix} \tag{22}
$$
$$
\boldsymbol{\psi}_{1,\mathrm{s}} = -\boldsymbol{B_4}^{-1}(2\pi\boldsymbol{I} - \boldsymbol{A_4})\left[\alpha\boldsymbol{\phi}_{1,\mathrm{b}} + \boldsymbol{F}\right] \tag{23}
$$

The values $\boldsymbol{\psi}_{1,\mathrm{b}}$ and $\boldsymbol{\phi}_{1,\mathrm{s}}$ are obtained by solving the matrix system of equation (22). The potential $\boldsymbol{\phi}_{2,\mathrm{s}}$ may then be obtained from the relation $\boldsymbol{\phi}_{2,\mathrm{s}} = \boldsymbol{F} + \alpha\boldsymbol{\phi}_1$. Finally, the tangential velocities, $\partial\boldsymbol{\phi}_{1,\mathrm{b}}/\partial s$, $\partial\boldsymbol{\phi}_{1,\mathrm{s}}/\partial s$ and $\partial\boldsymbol{\phi}_{2,\mathrm{s}}/\partial s$, are calculated based on the potentials at the node points and the geometry of the boundaries using cubic spline interpolations. With both the normal and tangential velocities known at each node, the boundaries of the domain are updated in time using equation (10). Similarly, $\boldsymbol{\phi}_{1,\mathrm{b}}$ and $\boldsymbol{F}$ are updated with equations (8) and (9), respectively.

4.4. Initial conditions

The initial conditions determine the values of the potentials on the bubble surface and at the fluid-fluid interface at the beginning of the simulation. We consider that the fluid-fluid interface is initially at rest, meaning that the potential $\phi_{1,\mathrm{s}}(t_0) = \phi_{2,\mathrm{s}}(t_0) = 0$ and therefore $F(t_0) = 0$, where t_0 is the initial time. On the surface of the bubble, two sets of initial conditions may be employed depending on the gas content of the bubble. This choice is left to the user before the beginning the simulations. If one wishes to model a cavitation bubble filled exclusively with liquid vapor, the earliest stage of its growth can be approximated by the Rayleigh model [6], which is assumed to also hold by symmetry for the growth phase of a spherical bubble in an unconfined medium. The approximation of initial sphericity is not unreasonable as nearby boundaries have little effect on the bubble behavior within the first instants of its lifetime. In that case, the bubble is initiated as a sphere of radius $R_0 = 0.1 R_\mathrm{m}$, as suggested by Blake et al. [25]. Note that the dimensionless value of R_m is unity. The corresponding initial time, t_0, and potential, $\phi_{1,\mathrm{b}}(t_0)$, are derived from the Rayleigh equation for a growing bubble. These values of are listed below in non-dimensional units,

$$
t_0 = 0.0015527 \quad \text{and} \quad \phi_{1,\mathrm{b}}(t_0) = -2.580698 \tag{24}
$$

If one wishes to include the presence of non-condensible gas, we consider the bubble as an initially stationary high-pressure gas cavity whose earliest stage of growth is approximated by the dimensionless Rayleigh-Plesset equation,

$$
R\ddot{R} + \frac{3}{2}\dot{R}^2 = \epsilon\left(\frac{R_0}{R}\right)^{3k} - 1 \tag{25}
$$

where the over-dots indicate the temporal derivatives. At time $t_0 = 0$, the potential on the bubble is given by $\phi_{1,\mathrm{b}}(t_0) = 0$. By further imposing that the maximum dimensionless radius reached by this bubble in an infinite medium is unity, the relation between R_0, ϵ and k may be derived from the Rayleigh-Plesset equation and is given by [36,59,37],

$$
\frac{\epsilon}{k-1}(R_0^{3k} - R_0^3) = R_0^3 - 1 \tag{26}
$$

A root-finding algorithm [47] is used to establish the value of R_0 based on the values of ϵ and k provided by the user.

4.5. Time-stepping

Once all potentials and velocities are known at time $t = t_n$, equations (8), (9) and (10) are advanced in time. We have included two temporal

schemes to update the different quantities, noted here y. The scheme is to be chosen by the user before beginning the simulations. A first order explicit Euler time step is implemented to allow fast computations. It uses a constant approximation of the derivative $f = dy/dt$ at time t_n so that the value of y at time $t_n + \Delta t$ is given by,

$$
y(t_n + \Delta t) = y(t_n) + \Delta t f(t_n, y_n) \tag{27}
$$

For increased accuracy and stability, the second order Heun's method is also implemented. In that case, the value of y at time $t_n + \Delta t$ is given by,

$$
y(t_n + \Delta t) = y(t_n) + \frac{\Delta t}{2}\left[f(t_n, y_n) + f(t_n + \Delta t, y(t_n) + \Delta t f(t_n, y_n))\right] \tag{28}
$$

For both time-stepping schemes, we use adaptive time steps. This ensures that small time steps are used when high flow velocities occur, which is usually the case in the first moments of bubble growth or the last instants of its collapse, and that larger time steps are used around the instants when the bubble reaches its maximum volume, where the flow velocities are much slower. Following the work of Curtiss [53], we define the value of Δt to limit the maximum change in potential over the bubble boundary or at the fluid-fluid interface,

$$
\Delta t = \max\left[\min\left(\frac{\Delta\theta}{\max\left[\max\left(|\frac{D\phi_1}{Dt}|\right), \max\left(|\frac{DF}{Dt}|\right)\right]}, \Delta t_\mathrm{max}\right), \Delta t_\mathrm{min}\right] \tag{29}
$$

where $\Delta\theta$ is a constant chosen by the user on a case by case basis. A maximum time step size is additionally imposed in the computation to avoid a loss of stability, $\Delta t_\mathrm{max} = 0.01$, as well as a minimum value of this time step set at $\Delta t_\mathrm{min} = 10^{-5}$. The latter is implemented to limit the effect of numerical noise as well as smoothing and filtering effects, which may become preponderant when very small time steps are used [53].

4.6. Curvature computation

The computation of the curvature is required to account for elastic effects at the fluid-fluid interface. In an axisymmetric configuration, it may be calculated as a function of the spatial derivatives of the coordinates $r(\xi)$ and $z(\xi)$,

$$
\bar{K} = \begin{cases} \dfrac{r'z'' - z'r''}{(r'^2 + z'^2)^{3/2}} + \dfrac{z'}{r(r'^2 + z'^2)^{1/2}} & \text{if } r \neq 0, \\ \dfrac{2(r'z'' - z'r'')}{(r'^2 + z'^2)^{3/2}} & \text{if } r = 0 \end{cases} \tag{30}
$$

The values of the various spatial derivatives (noted with prime symbols) are estimated by a fourth order polynomial fitted over 9 points around the node of interest. The spatial derivatives of this polynomial are then used in equation (30). This technique was proposed by Curtiss [53] to achieve higher stability compared to the spatial derivative obtained from spline interpolations. We use the function *polyfit* of the Armadillo library to efficiently construct the polynomials [45,46].

4.7. Re-meshing

The Lagrangian nature of the simulation implies that the nodes on the bubble surface and the fluid-fluid interface are advected by the fluid velocity and may end up clustering around region of high curvature and high flow velocities. This may lead to difficulties associated with the integration of equations (15) and (16) as well as leave certain regions of the boundaries under-resolved. We avoid this by re-meshing the bubble and the fluid-fluid interface at each time step. The N nodes are re-gridded using a geometric progression, in which case their positions, ξ_i, along the surfaces of total arc-length S are given by,
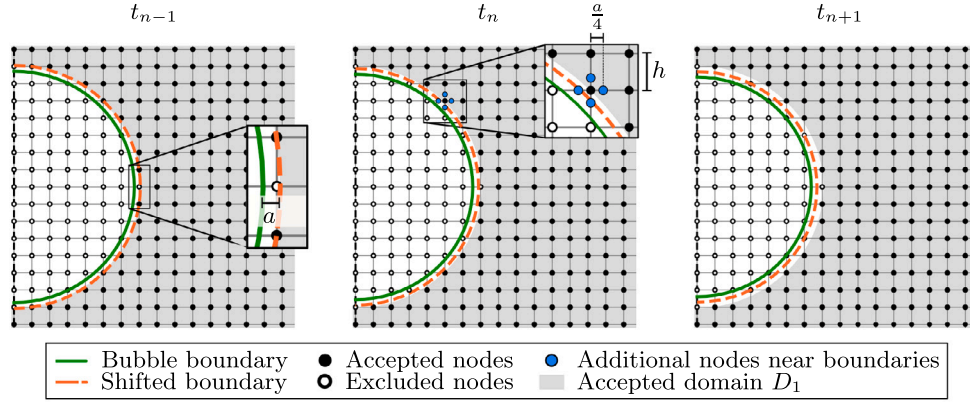
Fig. 3. Meshing of the computational domain D_1. Three successive instants of the collapse of a spherical cavity are shown at time points t_{n-1}, t_n and t_{n+1}. The solid green line illustrates the boundary of the fluid region defined by the cavity, and the dashed orange line shows the same boundary shifted by the user-defined quantity a. The filled black markers indicate grid points that lie within the newly defined fluid domain (i.e. defined by the orange dashed boundary) at times t_{n-1}, t_n and t_{n+1}. For grid point laying adjacent to the domain boundaries, additional grid nodes are generated so that finite-differences may be conducted on a five-point stencil. The later is indicated by blue circular markers in the zoomed box. (For interpretation of the colors in the figure(s), the reader is referred to the web version of this article.)

$$\xi_i = \begin{cases} 0 & \text{if } i = 1, \\ hS \sum_{k=2}^{i} r^{k-2} & \text{if } i = 2, 3, ..., N \end{cases} \tag{31}$$

where $h = (r-1)/(r^{(N-1)} - 1)$ is the first grid spacing with r the ratio of the geometric progression. On the bubble surface we find that uniformly distributed grid points give satisfactory results in most cases and therefore set $r = 0.9999$. At the fluid-fluid interface, we concentrate the node density around the symmetry axis, where the deformation is largest, and use $r = 0.97$.

4.8. Smoothing

As observed in previous works [32,56,36,53], numerical instabilities may develop on the boundaries of the domain. If left untreated, these may grow and lead to a saw-tooth shape of the bubble surface and/or fluid-fluid interface. To prevent the occurrence of such instabilities, the boundaries surfaces are smoothed using a five point smoothing formula proposed by Longuet-Higgins and Cokelet [60] and extended to handle unevenly spaced nodes. The frequency at which the boundaries are smoothed is left to user.

4.9. End of simulation

The model computes the bubble dynamics as long as its surface remains simply connected. In most cases, this means that the simulation ends at the moment when the liquid micro-jet that forms and travels along the symmetry axis of the bubble hits its opposite side, i.e. when the bubble becomes toroidal. Right after this instant, the fluid domain is doubly connected and the solution procedure described above is no longer applicable. Although numerical methods have been developed to simulate toroidal bubble dynamics (see for instance the work of Wang et al. [32]), these are not implemented in the current version of our solver, which we believe is adequate to capture most features of the bubble first oscillation. As a result, a condition to detect any intersection of the bubble surface is checked after each time step.

4.10. Flow field quantities: second processing stage

In a secondary processing phase, we additionally provide the option to calculate the velocity and pressure fields in the fluid domain D_1 at any time step, t_n. These quantities are evaluated at discrete location in the domain $D_1 \setminus \partial D_1$, meshed on a structured grid with equidistant nodes (note that such a grid is not needed for the first processing phase). We evaluate the values of the potentials ϕ_1 at any grid point

by solving equation (11), taking $c_1(\mathbf{y}) = 4\pi$ for $\mathbf{y} \in D_1 \setminus \partial D_1$. The flow velocities are then obtained as $(u, v) = (\partial\phi_1/\partial r, \partial\phi_1/\partial z)$ using a central differencing scheme on a five point stencil,

$$u_{i,j} = \frac{\phi_{i+1,j} - \phi_{i-1,j}}{2h} \tag{32}$$

$$v_{i,j} = \frac{\phi_{i,j+1} - \phi_{i,j-1}}{2h} \tag{33}$$

where h is the spacing between nodes and the subscripts i and j refer to an arbitrary node point in $D_1 \setminus \partial D_1$. Alternatively, the pressures are computed from the dimensionless Bernoulli equation valid in D_1,

$$\frac{\partial\phi_1}{\partial t} + \frac{|\nabla\phi_1|^2}{2} + P_1 + \delta(z_1 - z_0) - 1 = 0 \tag{34}$$

where P_1 is the dimensionless pressure. The presence of temporal derivative in equation (34) implies that the potentials must also be evaluated at different time steps around t_n. We choose a 3-point central difference scheme to calculate the potential temporal derivative,

$$\frac{\partial\phi_{i,j}}{\partial t} = \frac{\Delta t_1^2 \phi_{i,j,t_{n+1}} + (\Delta t_2^2 - \Delta t_1^2)\phi_{i,j,t_n} - \Delta t_2^2 \phi_{i,j,t_{n-1}}}{\Delta t_2 \Delta t_1 (\Delta t_2 + \Delta t_1)} \tag{35}$$

where $\Delta t_1 = t_n - t_{n-1}$ and $\Delta t_2 = t_{n+1} - t_n$. Note that the 3-point central difference scheme requires the potentials to be known at time t_{n+1}. This implies that equation (35) can only be solved in a secondary processing phase, once the potentials on the domain boundaries have been evaluated for the entire lifetime of the bubble.

To ensure that each node where the potential is evaluated remains bounded within the fluid domains $D_{1,n-1}$, $D_{1,n}$ and $D_{1,n+1}$ at times t_{n-1}, t_n and t_{n+1}, respectively, the temporal evolution of the boundaries of D_1 must be considered. The procedure to achieve this is illustrated in Fig. 3, which shows the boundary (solid green line) of a spherically collapsing cavity at three successive times. First, the boundary at time t_n is shifted away from the original boundary by a user-defined constant quantity, a. The newly defined boundary is illustrated with an orange dashed line. This adjustment ensures that the grid points in the fluid domain are taken at a certain distance from the nodes constituting the actual domain boundaries (bubble and fluid-fluid interface), thus avoiding inaccuracies in the evaluation of the integrals in equation (11) that could occur in the case of excessive proximity. Next, a *point-in-polygon* problem is solved using a *winding number* algorithm to select the grid points that lie within this modified domain. The same process is repeated at times t_{n-1} and t_{n+1}. The grid points accepted over all three time steps are indicated with black filled markers in Fig. 3, while the grids points outside the domain are indicated with hollow circular markers. Finally,

Algorithm 1 Solution procedure for the main processing stage.

1: **Inputs:**
    Read the input file;
2: **Initialize:**
    Assign the initial nodes position (r_0, z_0) and associated
    potential values $\phi_{0,b}$ and F_0;
3: **while** intersection = False **do**   ▷ Simulation stops if the bubble surface
                                      is intersected.
4:     **for** i in $N_b + N_s + 2$ **do**
5:         **for** j in $N_b + N_s + 2$ **do**
6:             Compute the elements A_{ij} and B_{ij} of the coefficient matrices;
7:         **end for**
8:     **end for**
9:     Compute the normal velocities ψ_b and $\psi_{1,s}$ and the potentials
        $\phi_{1,s}$ and $\phi_{2,s}$;
10:     Compute the tangential velocities $\partial\phi_b/\partial s$, $\partial\phi_{1,s}/\partial s$ and $\partial\phi_{2,s}/\partial s$;
11:     Compute the bubble volume V;
12:     **if** elasticity **then**   ▷ Only if surface tension is considered.
13:         Compute the fluid-fluid interface curvature $\tilde{K}$;
14:     **end if**
15:     Update the values of ϕ_b and F;
16:     Update the position of the nodes (r, z);
17:     **if** smoothing **then**   ▷ Smoothing is applied every N time steps.
18:         Smooth the bubble surface and fluid-fluid interface;
19:     **end if**
20:     Re-mesh boundaries;
21:     Check for bubble intersection;
22:     Write solution to file;
23: **end while**

---

to also compute the finite-differences on a five-point stencil at the nodes adjacent to the domain boundaries, we create additional grid nodes at a distance $a/4$ from the grid point of interest (blue markers in the zoomed box of Fig. 3).

4.11. Solution procedure

In the interest of clarity, we provide a step-by-step overview of the solution procedure for the main processing stage, summarized in Algorithm 1. A set of initial conditions is provided by the user in an input file that is read by the main program. This file contains information about the spatial discretization, the temporal integration scheme, and the physical parameters that determine the dynamics of the bubbles. Based on the input data, the main solver initializes the simulation by discretizing the domain boundaries and assigning a potential $\phi_{b,0}$ to each node on the bubble surface and a potential difference F_0 to each node at the fluid-fluid interface. The solver then computes the elements of the coefficient matrices $\boldsymbol{A}$ and $\boldsymbol{B}$ using the equations (15) and (16), respectively. At this stage, the normal velocities ψ_b and $\psi_{1,s}$ as well as the potential $\phi_{1,s}$ can be obtained by solving the equations (22) and (23). The potential $\phi_{2,s}$ is found via the relation $\phi_{2,s} = F - \alpha\phi_1$. The tangential velocities are derived from the potentials on the boundaries. The bubble volume and, depending on the simulation inputs, the curvature of the fluid-fluid interface are also calculated at this stage. The potentials ϕ_b and F are then updated in time with the equations (8) and (9), and the position of the nodes with the equation (10). Depending on the smoothing frequency chosen by the user, the boundaries can be filtered to avoid the onset of numerical instabilities. Finally, the bubble and fluid-fluid interface surfaces are re-meshed to avoid a clustering of the node points. The calculation is performed until the originally spherical bubble becomes toroidal or splits into two or more separate bubbles. At each time step, the position, potential value, and normal velocity of each node on the bubble and fluid-fluid surface are stored in an output file for post-processing. The volume evolution of the bubble is also stored.

After this simulation, the user can choose to calculate the velocity and pressure fields at any of the calculated time steps. This is done in the secondary processing stage with a Python script that uses the output file of the main processing stage as input for the new calculation.

5. Validation

5.1. Comparison with analytical solutions

We begin by assessing the validity and accuracy of the numerical implementation described above by comparing the BIM calculations with analytical solutions of a spherically oscillating bubble in an infinite medium. In this configuration, the fluid-fluid interface should have no influence on the bubble dynamics. This is achieved by setting the densities on both sides of the interface equal, i.e. $\alpha = 1$. The effects of gravity are also neglected. The bubbles considered in this section are discretized in 40 elements and are located at a distance $\gamma = 1$ from the fluid-fluid interface, which itself is discretized in 60 elements. A value of $\Delta\theta = 0.01$ is chosen for the time steps and smoothing is applied every eight time steps. Finally, unless otherwise stated, the second-order time integration scheme is used.

5.1.1. Rayleigh bubble

We first consider the dynamics of a vapor bubble. Given the initial conditions assumed for such a bubble, the time evolution of its radius is expected to follow that predicted by the Rayleigh model, mirrored across the axis at $t = t_R \approx 0.915$. This evolution is illustrated in Fig. 4(a) which demonstrates a very good agreement between the radius calculated with the BIM simulation and the radius obtained by solving the Rayleigh equation. Moreover, an originally spherical bubble should remain spherical in an infinite medium. Thus, any deviation from sphericity is a consequence of numerical noise. We assess this deviation with the following formula which computes the maximum difference between the radius at a node and the averaged radius of all nodes [58],

$$d_{sph} = \max\left(\frac{|R_i - R_{avg}|}{R_{avg}}\right) \tag{36}$$

where $R_i = \sqrt{r_i^2 + (z_i + \gamma)^2}$ is the distance between the bubble center, located at γ, and the ith node on the bubble surface and R_{avg} represents this same distance but averaged over all the nodes. Note that $z_i < 0$. We apply equation (36) at every time step of the simulation, the results of which are shown in Fig. 4(b). The maximum deviation from sphericity remains below a tenth of a percent, indicative of a bubble retaining a very high sphericity throughout its lifetime. We nevertheless note that the deviation increases at the end of the collapse, i.e. around $t \approx 1.83$, where the radius of the bubble tends towards zero. This is likely because the nodes that make up the bubble surface become very close to each other, leading to inaccuracies and instabilities in the calculation of the boundary integrals [58].

Fig. 5(a) shows the BIM computation of the velocity and pressure fields in the liquid phase associated with the same bubble at time $t = 1.815$. The analytical solutions for the radial distribution the liquid velocity and pressure fields induced by a collapsing Rayleigh bubble are known and can be derived from the liquid continuity and momentum equations. These are expressed as follows in dimensionless form for a bubble whose maximum radius is unity,

$$U(r,t) = \sqrt{\frac{2}{3}\left(\frac{1}{R^3} - 1\right)}\frac{R^2}{r^2} \quad \forall r \geq R \tag{37}$$

$$P(r,t) = 1 + \frac{R}{3r}\left(\frac{1}{R^3} - 4\right) - \frac{R^4}{3r^4}\left(\frac{1}{R^3} - 1\right) \quad \forall r \geq R \tag{38}$$

where $R = R(t)$ denotes the bubble radius evolution as predicted by the Rayleigh model and r is the distance from the bubble center. Fig. 5(a) shows the BIM computation of the velocity and pressure field associated with a collapsing bubble at time $t = 1.815$. The computed velocity and pressure radial evolution are compared to the analytical solutions to equations (37) and (38) in Figs. 5(b) and 5(c), respectively. For both quantities, we observe an excellent agreement.
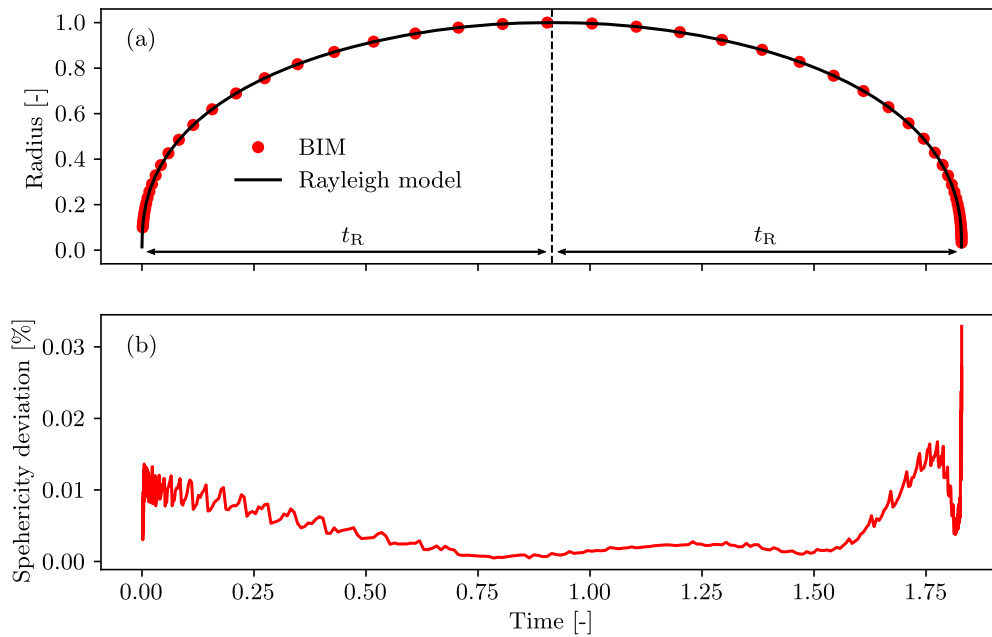
Fig. 4. (a) Temporal evolution of the vapor bubble averaged radius. The circular markers represent the solution of the BIM simulation and the solid line shows the solution of the Rayleigh model mirrored across the axis at $t = t_R \approx 0.915$, indicated with a dashed line. (b) Temporal evolution of the maximum deviation from the averaged radius for the bubble obtained with the BIM simulation. The following additional dimensionless parameters are considered in the simulation: $\epsilon = 0$, $\delta = 0$ and $\alpha = 1$.
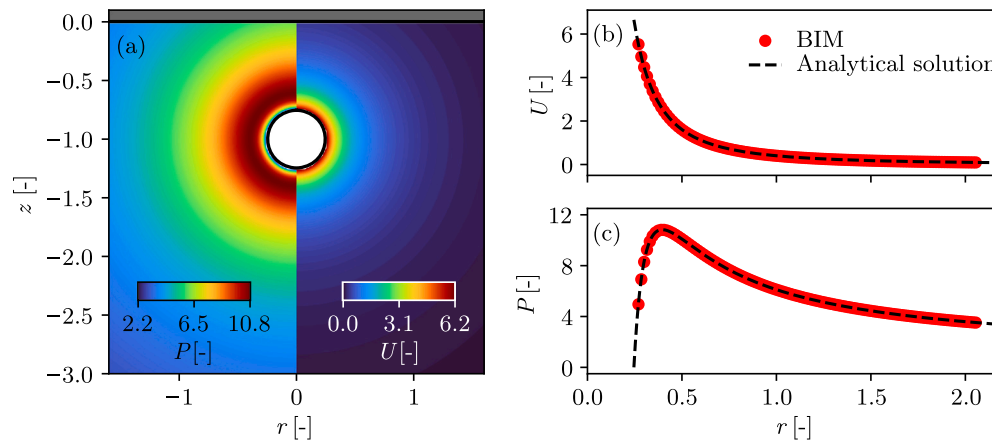
Fig. 5. (a) Computed pressure (left) and velocity (right) fields induced by a collapsing vapor bubble at time $t = 1.815$. The black line around $z = 0$ indicates the position of the fluid-fluid interface and the gray zone at $z > 0$ represents the second fluid for which the flow field quantities are not computed. (b) Comparison of the computed and analytical velocity fields along the radial direction taking $z = -1$. (c) Comparison of the computed and analytical pressure fields along the radial direction taking $z = -1$. The following dimensionless parameters are considered in the simulation: $\epsilon = 0$, $\delta = 0$ and $\alpha = 1$ and $\gamma = 1$.

5.1.2. Rayleigh-Plesset bubble

We now consider a bubble filled with liquid vapor and non-condensable gas. Fig. 6(a) shows the 3 first oscillations of a bubble with strength parameter $\epsilon = 100$ and specific heat ratio $k = 1.4$. The BIM simulation is compared to the solution of the Rayleigh-Plesset equation (see equation (25)) and we find a remarkable agreement. On Fig. 6(b), we use equation (36) to assess the maximum deviation from sphericity of a bubble with strength parameter $\epsilon = 100$ and another one with $\epsilon = 1000$. Overall, both bubbles exhibit excellent spherical symmetry with an average maximum deviation over the 3 first oscillation of 0.3% for the bubble with $\epsilon = 100$ and 0.37% for the bubble with $\epsilon = 1000$. However, we observe spikes in the maximum deviation from sphericity when the bubbles reach their respective minimum volumes (at $t \approx 1.94, 3.89, 5.83$ for the bubble with $\epsilon = 100$ and $t \approx 1.87, 3.74, 5.61$ for the bubble $\epsilon = 1000$). These are attributed to the nodes on the bubble surface being very close to each other at these instants, which can lead to errors in the evaluation of the boundary integrals [58]. Smooth-

ing prevents these instabilities from growing after the first and second collapse and the simulation remains stable. Nevertheless, after the third bubble collapse, the growing and accumulated numerical instabilities are such that both simulations diverge despite the surface smoothing.

Although this surface smoothing can prevent the onset of instabilities, it can also lead to undesirable energy and/or mass variations. The re-meshing of the interface nodes as well as an inappropriate temporal integration scheme and time step size may also contribute to this undesirable effect. We therefore evaluate the accuracy of BIMBAMBUM in this respect by considering the first two oscillation periods of a spherical, non-buoyant bubble filled with liquid vapor and non-condensable gas and analyze the associated energy conservation. In this configuration, the total energy of the bubble system consists of the potential energy and the kinetic energy, $E_{tot} = E_p + E_k$. The definition of these quantities can be found in the work of Wang [61]. Considering the non-viscous and incompressible nature of the problem, the total energy must be conserved throughout the bubble lifetime, and any change in the lat-
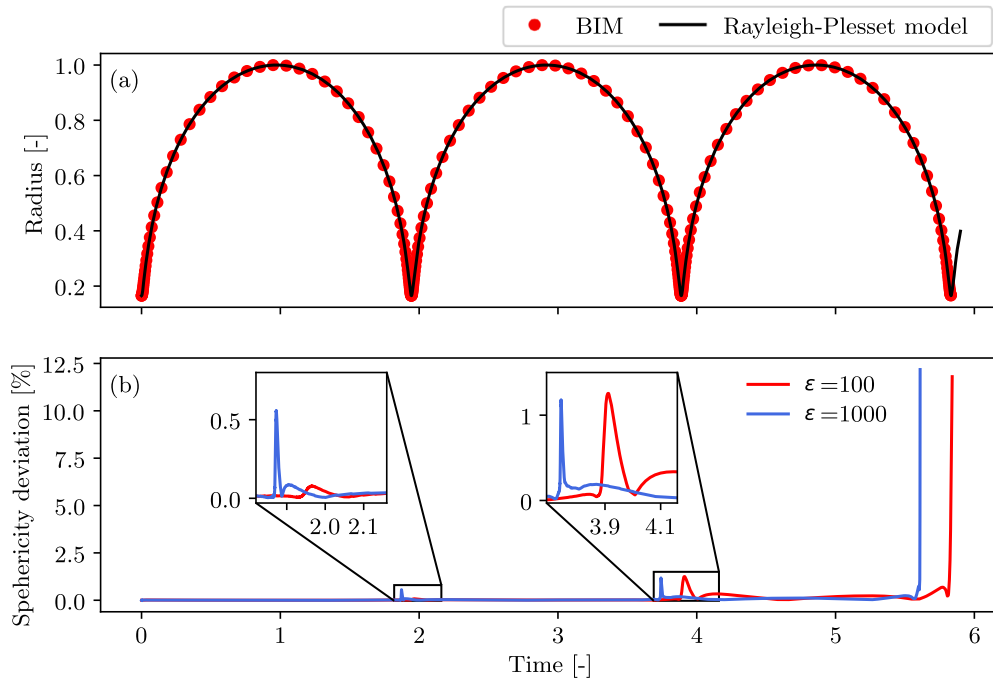
Fig. 6. (a) Temporal evolution of the bubble averaged radius. The bubble under consideration is filled with vapor and non-condensable gas, with a strength parameter $\epsilon = 100$. The circular markers represent the solution of the BIM simulation and the solid lines show the solution of the Rayleigh-Plesset model. (b) Temporal evolution of the maximum deviation from the averaged radius for bubbles obtained with the BIM simulation with two distinct strength parameters: $\epsilon = 100$ and $\epsilon = 1000$. The peaks in the maximum deviation occur when the bubbles reach their respective minimum radius. The following additional dimensionless parameters are considered in the simulation: $\delta = 0$ and $\alpha = 1$ and $\gamma = 1.0$.
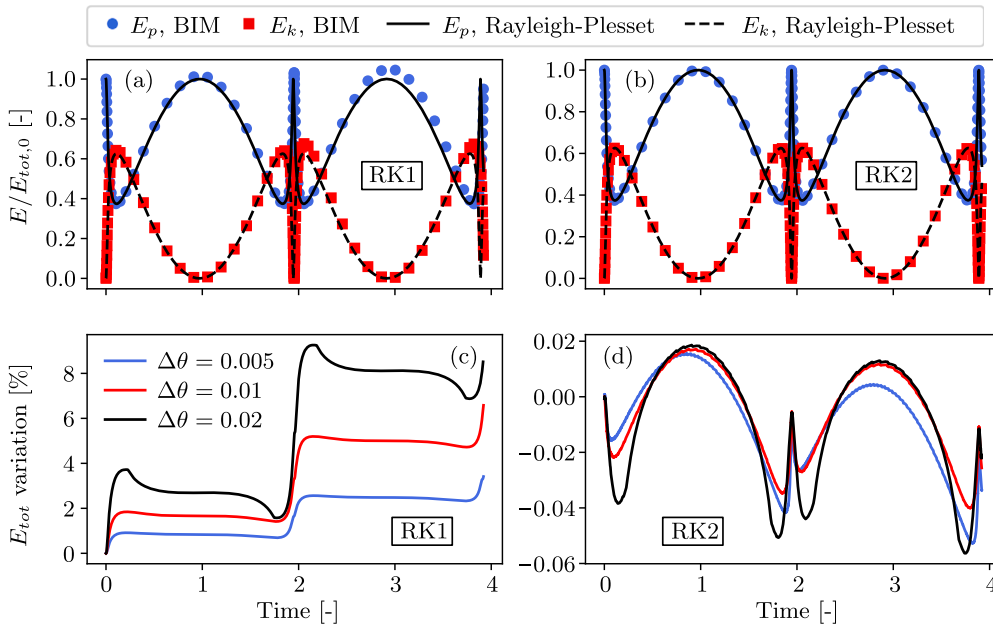

Fig. 7. (a) and (b) Temporal evolution of the potential and kinetic energy of a spherical bubble filled with vapor and non-condensable gas, computed with the first-order (RK1) and second-order (RK2) time integration schemes (strength parameter $\epsilon = 100$ and time step constant $\Delta\theta = 0.01$). The markers indicate the solution of the BIM simulations and the lines show solutions obtained by solving the Rayleigh-Plesset equation for the bubble dynamics over its first two oscillation periods. (c) and (d) Variation of the bubble total energy for different $\Delta\theta$ values, computed with the first-order (RK1) and second-order (RK2) time integration schemes. A non-zero total energy variation indicates inaccuracies in the numerical scheme.

ter would be due to numerical errors. Figs. 7(a) and 7(b) show the evolution of the potential and kinetic energy of such a bubble with the strength parameter $\epsilon = 100$, whose dynamics were calculated using the first (RK1) and second-order (RK2) time integration schemes, respectively. The results of the BIM simulations are compared to the energies obtained by solving the Rayleigh-Plesset equation for the bubble

dynamics. We observe an excellent agreement between the theoretical and second-order BIM solution, but discrepancies when the first-order scheme is used. To quantify those discrepancies, we show in Figs. 7(c) and 7(d) the relative change in total energy for different values of the time constant $\Delta\theta$ (see equation (29)) and the two different temporal integration schemes. It is evident that the use of the first-order tempo-
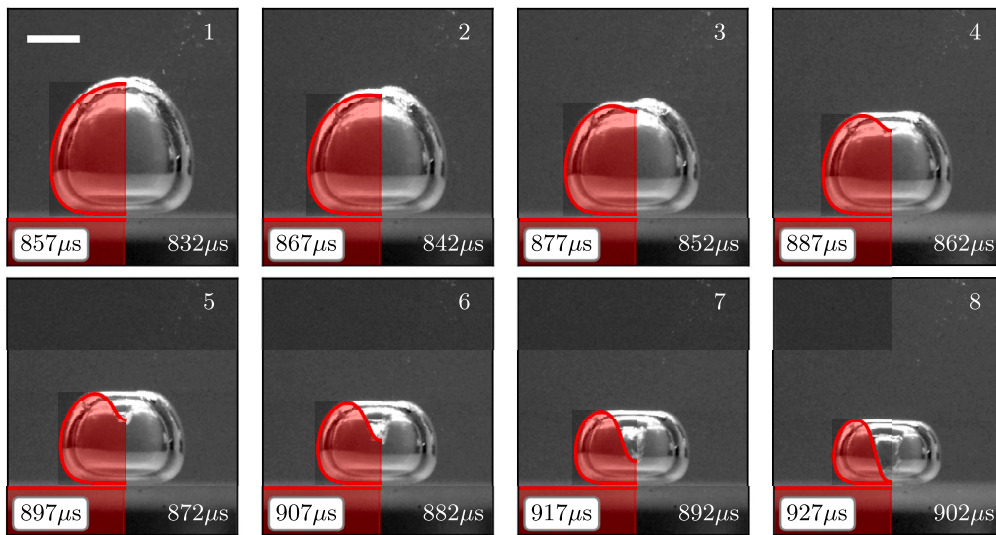
Fig. 8. Comparison between the experimental and numerical results for a vapor cavitation bubble in the vicinity of a rigid boundary at $\gamma = 0.95$. The simulation is superposed on the left halve of the frames. The experimental image sequence highlights the formation of the bubble's micro-jet. The laser-induced bubble has a maximum radius $R_m \approx 4.4$ mm and the image sequence is initiated 832 µs after the bubble generation. The times of the numerical simulation are shifted by 25 µs with respect to the experiment so that the spatiotemporal evolution of the bubbles may be compared. The following additional dimensionless parameters are considered in the simulation: $\delta = 0$, $\alpha = 0.001$ and $\epsilon = 0$. The white line indicates the 2 mm scale.

ral integration scheme with large $\Delta\theta$ values does not conserve the total energy and leads to unacceptable results, especially during the second oscillation period. On the other hand, the second-order temporal integration scheme provides accurate results with little change in the total energy of the bubble system. Care must therefore be taken when choosing these simulation parameters.

5.2. Comparison with experiments and other numerical implementations

5.2.1. Rigid boundary

The dynamics of a cavitation bubble near a rigid boundary is substantially different to that of an unbounded bubble. Such a bubble exhibits an aspherical collapse together with the formation of a liquid micro-jet directed toward the rigid boundary. We test the BIM solver against the experiment of a laser-induced cavitation bubbles collapsing in the vicinity of a thick aluminum plate. Details pertaining to the experimental setup can be found in the references [42,43]. The laser-induced bubble has a maximum radius $R_m \approx 4.4$ mm and is generated at a stand-off distance $\gamma \approx 0.95$. In the simulation, we consider a vapor bubble which we discretize with $N_b = 80$ elements. Later, we will justify this choice of discretization. The fluid-fluid interface is discretized with $N_s = 60$ elements. In accordance with the work of Klaseboer and Khoo [36], we moreover use $\alpha = 0.001$ to model the rigid boundary.

Fig. 8 shows an image sequence that focuses on the formation of the micro-jet and its displacement within the bubble. The sequence is initiated 832 µs after the bubble generation and exhibits the following 70 µs of its lifetime at the end of which the micro-jet impacts onto the bubble's lower hemisphere. The simulations overestimate the instant of jet impact by roughly 25 µs, which corresponds to a relative error of 2.8% with respect to the experiment. Therefore, to compare the spatiotemporal evolution of the two bubbles profile, we superimpose the simulations results on the left halves of the frames, shifted by 25 µs. Apart from the temporal shift, we find a close qualitative agreement between the two dynamics and conclude that the simulation reproduces the experiment quite well despite the simplifying assumptions of the physical model, such as the exclusion of compressibility or viscosity effects.

The discretization of the boundaries of the numerical domain can significantly influence the accuracy of the solver. In the case of a bubble near a rigid boundary, this is especially true for the choice of elements on the bubble surface, N_b. In Fig. 9, we perform a convergence study

to assess the influence of this parameter on the numerical solution. Fig. 9(a) shows the bubble profile at dimensionless time $t = 2.0864$ for different values of N_b. There is a notable difference in the position of the micro-jet tip, suggesting that the timing of the jet impact on the lower bubble hemisphere and its velocity may be miscalculated if an inadequate discretization is employed. The timing of the jet impact for the different discretizations is shown in Fig. 9(b). The figure illustrates a clear convergence of this feature of the bubble dynamics where the relative difference between the $N_b = 80$ and $N_b = 100$ disctretizations is less than 0.02%. Increasing the value of N_b, however, is also associated with an increased computational cost, which we depict in Fig. 9(b). The results, which were performed on a single core of a laptop computer (the processor of the computer is an Apple M1 chip), show that the calculation time increases from about 4 minutes for $N_b = 20$ to about 17 minutes for $N_b = 100$. Nevertheless, these calculation times can be significantly reduced if the user executes the code in parallel through the OpenMP library [48], as can be seen in Fig. 9(c), where the execution of the solver on 8 threads can reduce the computation time by a factor of 7.3 (these tests were conducted on a computer equipped with an Intel Xeon E5-2630v4 processor).

5.2.2. Free surface

Cavitation bubbles oscillating near a free surface also exhibit a micro-jet during their collapse, which differs from the jet formed near a rigid wall mainly in that it is directed away from the adjacent boundary. Depending on the distance, the free surface can also deform drastically resulting in the formation of liquid spikes.

We compare the prediction of the BIM to the experiment of a laser-induced cavitation bubble with $R_m \approx 2.4$ mm generated at $\gamma \approx 0.75$ from a water-air interface. We consider a vapor bubble in the simulation and discretize both the fluid-fluid interface and the bubble with 80 elements. To reproduce the density jump of the experiment, we use $\alpha = 1000$. A direct comparison between the experiment and the simulation is provided in Fig. 10, where the first frame is taken 22 µs after the bubble generation. Frames 1–4 depict the bubble growth and frames 5–8 its collapse until the micro-jets impact on the bubble lower hemisphere. We observe an excellent agreement between the spatiotemporal evolution the bubble exterior shape, although the simulation underestimates the time to jet impact by 15 µs resulting in a relative error of 4.5% with respect to the experiment (frame 8).
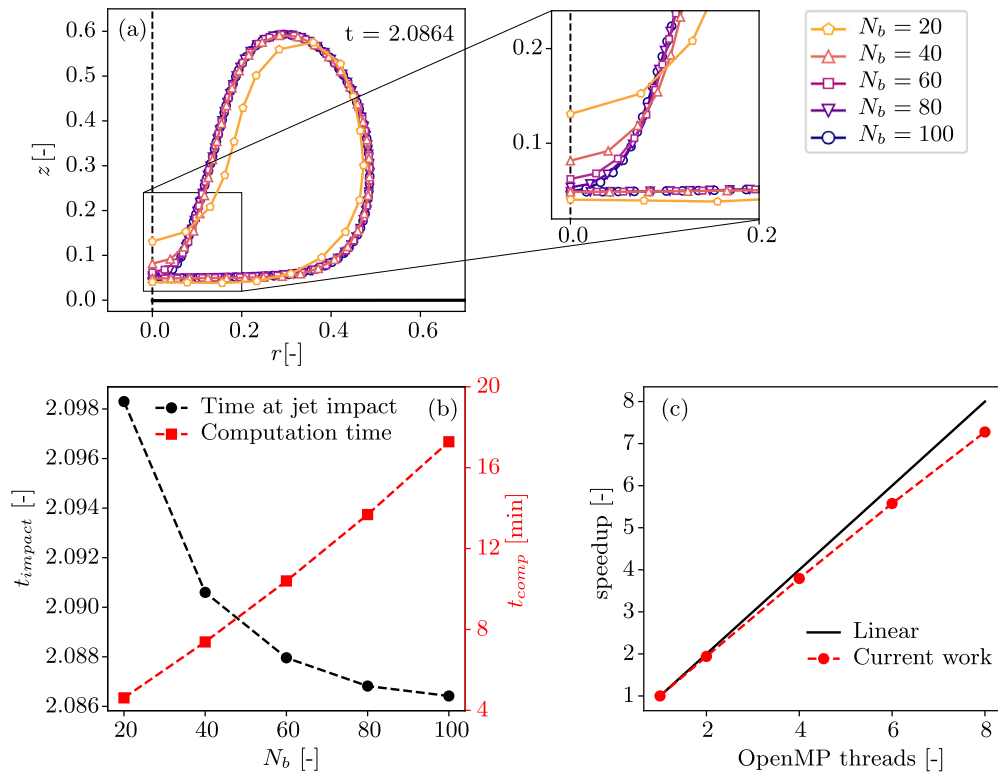
Fig. 9. (a) Convergence study of the bubble profile near a rigid boundary at $\gamma = 0.95$ at dimensionless time $t = 2.0864$ for different discretizations N_b and (b) convergence study of the dimensionless time of micro-jet impact on the bubble's lower hemisphere for the different discretizations, with the associated computation time. The simulations were performed on a single core of a laptop computer (the processor of the computer is an Apple M1 chip). (c) Speedup of the computation time relative to serial processing achieved through parallelization of the performance-critical tasks with the OpenMP library [48]. The speedup tests were conducted on a computer equipped with a 10-core Intel Xeon E5-2630v4 processor and for a bubble discretized in $N_b = 80$ elements. A linear speedup curve is included for reference.
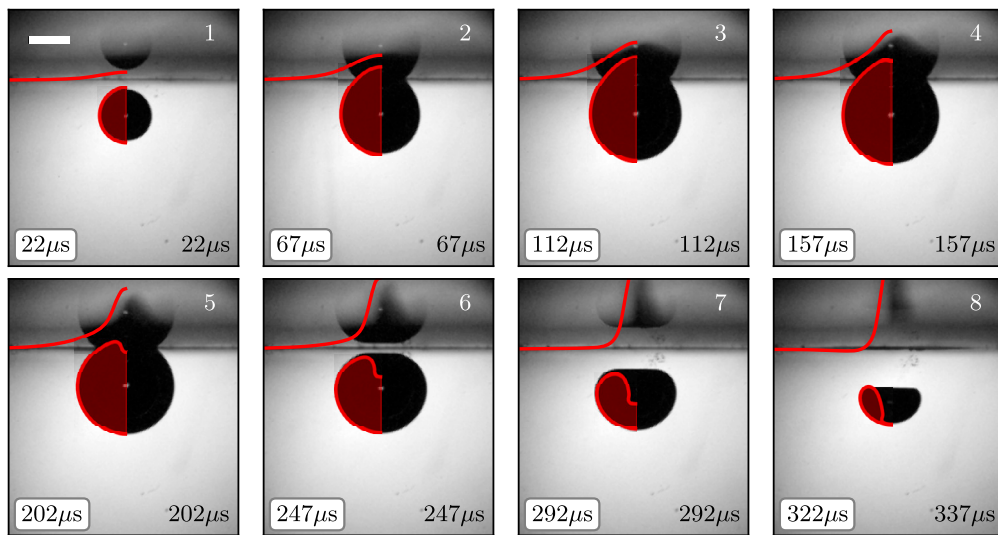

Fig. 10. Comparison between the experimental and numerical results for a vapor cavitation bubble in the vicinity of a free surface at $\gamma = 0.75$. The simulation is superposed on the left halve of the frames. The experimental image sequence depicts the growth (frames 1–4) and collapse (frames 5–8) of a laser-induced bubble with $R_m \approx 2.4$ mm. The timings of the numerical simulation and the experiment are identical for frames 1–7, but are shifted by 15 μs on frame 8 to allow comparison of the bubble profiles just before the micro-jet impact. The following additional dimensionless parameters are considered in the simulation: $\delta = 0$, $\alpha = 1000$ and $\epsilon = 0$. The white line indicates the 2 mm scale.
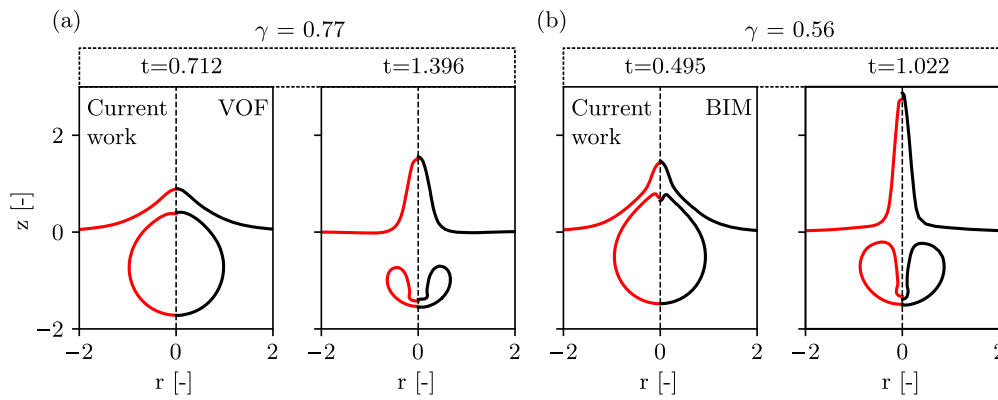
Fig. 11. Comparison between the current numerical results and other numerical results. (a) Comparison with the VOF simulation of Li et al. [62] (right halves of the frames) for a bubble filled with vapor and non-condensable gas near a free surface at $\gamma = 0.77$ at two dimensionless times. The following additional dimensionless parameters are considered in the simulation: $\alpha = 1000$, $\delta = 0.0018$, $\epsilon = 115$ and $k = 1.25$. (b) Comparison with the BIM simulation of Robinson et al. [33] (right halves of the frames) for a vapor cavitation bubble in the vicinity of a free surface at $\gamma = 0.56$ at two dimensionless times. The following additional dimensionless parameters are considered in the simulation: $\alpha = 1000$ and $\delta = 0.038$.

A direct evaluation of the micro-jet evolution within the bubble as well as the formation of the liquid spike predicted by the BIM is not possible due to the illumination technique employed in the experiment. Instead, we evaluate the validity of these features of the bubble by comparing our implementation of the BIM solver with other numerical results of bubbles oscillating near a free surface. First, we compare our BIM implementation with a compressible VOF (Volume of Fluid) simulation performed by Li et al. [62]. The authors considered a bubble located at a stand-off distance $\gamma = 0.77$ with a maximum reference radius of $R_m = 18.2$ mm. Their bubble is filled with gas with the specific heat ratio $k = 1.25$, is located in an environment with the pressure $p_\infty = 101325$ Pa and the initial pressure inside the bubble is set to $115 \times p_\infty$. As such, we choose the following parameters for our simulation: $\delta = 0.0018$, $\epsilon = 115$ and $k = 1.25$. The comparison of the two numerical simulations is illustrated on Fig. 11(a) for two dimensionless times: $t = 0.712$ and $t = 1.396$. The left halves of the frames show results from BIMBAMBUM and the right halves show the bubble profile extracted from the VOF simulation of Li et al. [62]. Both simulation results exhibit a good spatio-temporal agreement, which shows that our solver performs well compared to more elaborated numerical models. We then compare our BIM solver with that of Robinson et al. [33] for the case of a vapor bubble oscillating near a free surface at $\gamma = 0.56$. The reference experimental bubble on which these authors simulation is based reaches a maximum radius $R_m = 17.9$ mm in an environment with pressure $p_\infty = 6930$ Pa [63]. We therefore set $\delta = 0.038$. The comparison of the two numerical simulations is illustrated on Fig. 11(b) for two dimensionless times: $t = 0.495$ and $t = 1.022$. Again, the left halves of the frames show the current numerical implementation and the right halves show the bubble profile extracted from the BIM implementation of Robinson et al. [33]. Both bubbles display a very similar appearance, with the most notable difference being the position of the micro-jet tip and the height of the liquid spike. This difference, however small, could be explained by the use of different temporal schemes, spatial discretization or solution procedure.

6. Conclusion

We have presented the detailed implementation of BIMBAMBUM, a numerical flow solver designed to model the behavior of cavitation bubbles near an interface between two fluids. By adjusting the density ratio between the two fluids, different types of interfaces can be simulated, including rigid boundaries or free surfaces. In addition, a membrane-like elastic behavior of the fluid-fluid interface can be modeled through the inclusion of interfacial tension. Both fluids must satisfy Laplace's equation, so a boundary integral method can be used

to solve the flow problem by only discretizing the boundaries of the numerical domain.

We have validated the current implementation of the solver using theoretical solutions for the dynamics of spherical bubbles, experimental observations of cavitation bubbles collapsing near a rigid boundary and a free surface, and results from other simulation softwares that model the behavior of bubbles near free surfaces.

CRediT authorship contribution statement

Armand Baptiste Sieber: Conceptualization, Formal analysis, Methodology, Software, Validation, Writing – original draft, Writing – review & editing. **Henri Hugo Sieber:** Software, Writing – review & editing, Formal analysis, Methodology. **Davide Bernardo Preso:** Software, Validation, Writing – review & editing, Conceptualization, Formal analysis. **Mohamed Farhat:** Conceptualization, Formal analysis, Funding acquisition, Project administration, Resources, Supervision, Writing – review & editing.

Declaration of competing interest

The authors declare that they have no known competing financial interests or personal relationships that could have appeared to influence the work reported in this paper.

Data availability

The data that support the findings of this study are available from the corresponding author upon reasonable request.

Acknowledgements

Appendix A. Polynomial approximation of the complete elliptic integrals of the first and second kind

The complete elliptic integrals of the first and second kind, $K(k)$ and $E(k)$, respectively, are approximated with 12th order polynomials,

$$K(k) \approx P(1 - k^2) - Q(1 - k^2) \log(1 - k^2) \tag{A.1}$$

$$E(k) \approx R(1 - k^2) - S(1 - k^2) \log(1 - k^2) \tag{A.2}$$

The polynomials P, Q, R and S are expressed as $P(x) = \sum_{i=0}^{12} p_i x^i$, $Q(x) = \sum_{i=0}^{12} q_i x^i$, $R(x) = \sum_{i=0}^{12} r_i x^i$ and $S(x) = \sum_{i=0}^{12} s_i x^i$, respectively, and the associated tabulated coefficients are provided in Tables A.1 and A.2.

Table A.1
Tabulated polynomial coefficients for the approximation of the complete elliptic integral of the first kind.

p_0	1.3862943611198906188344642	q_0	0.5000000000000000000000000
p_1	0.0965735902799726547086616	q_1	0.1250000000000000000000000
p_2	0.0308851445324846182735965	q_2	0.0703125000000000000000000
p_3	0.0149376003697809868756849	q_3	0.0488281249999999987824278
p_4	0.0087663121986283512948673	q_4	0.0373840332029996524904238
p_5	0.0057548999165121183171308	q_5	0.0302810652677042043398923
p_6	0.0040681964891623595578422	q_6	0.0254437889627875149721937
p_7	0.0031671344811484017628661	q_7	0.0218963935859043951617029
p_8	0.0038591873504345181091441	q_8	0.0185969517204856628919574
p_9	0.0069724892720228755371054	q_9	0.0132664464229808055243329
p_{10}	0.0070003049842366187352619	q_{10}	0.0057215066512984512105679
p_{11}	0.0023553557623766313332515	q_{11}	0.0009874948865402974846014
p_{12}	0.0001617500382458658709102	q_{12}	0.0000351910715704804629391

Table A.2
Tabulated polynomial coefficients for the approximation of the complete elliptic integral of the second kind.

r_0	1.0000000000000000000000000	s_0	0.0000000000000000000000000
r_1	0.4431471805599453094172321	s_1	0.2500000000000000000000000
r_2	0.0568051927099794910314620	s_2	0.0937500000000000000000000
r_3	0.0218313704437371839613815	s_3	0.0585937499999999987183993
r_4	0.0115445214188370110354236	s_4	0.0427246093748680613212765
r_5	0.0071420131882050298706661	s_5	0.0336456281704939217515087
r_6	0.0048584665988127446359489	s_6	0.0277568883460602763157989
r_7	0.0036668034639439304538766	s_7	0.0235817963712635001858889
r_8	0.0042646942489190681351738	s_8	0.0198469981559132248161912
r_9	0.0074572701421245659618847	s_9	0.0140778319371711286211429
r_{10}	0.0074187134116304427753980	s_{10}	0.0060533000832926685582514
r_{11}	0.0024893354733649633990436	s_{11}	0.0010432120209879450926571
r_{12}	0.0001707651353968720443847	s_{12}	0.0000371478277891040153655

References

[1] R.E. Arndt, Cavitation in vortical flows, Annu. Rev. Fluid Mech. 34 (1) (2002) 143–175, https://doi.org/10.1146/annurev.fluid.34.082301.114957.

[2] A. Amini, M. Reclari, T. Sano, M. Iino, M. Farhat, Suppressing tip vortex cavitation by winglets, Exp. Fluids 60 (2019) 1–15, https://doi.org/10.1007/s00348-019-2809-z.

[3] E. Stride, C. Coussios, Nucleation, mapping and control of cavitation for drug delivery, Nat. Rev. Phys. 1 (8) (2019) 495–509, https://doi.org/10.1038/s42254-019-0074-y.

[4] M. Dular, T. Griessler-Bulc, I. Gutierrez-Aguirre, E. Heath, T. Kosjek, A.K. Klemenčič, M. Oder, M. Petkovšek, N. Rački, M. Ravnikar, et al., Use of hydrodynamic cavitation in (waste) water treatment, Ultrason. Sonochem. 29 (2016) 577–588.

[5] T. Yamashita, K. Ando, Low-intensity ultrasound induced cavitation and streaming in oxygen-supersaturated water: role of cavitation bubbles as physical cleaning agents, Ultrason. Sonochem. 52 (2019) 268–279, https://doi.org/10.1016/j.ultsonch.2018.11.025.

[6] L. Rayleigh, On the pressure developed in a liquid during the collapse of a spherical cavity, Lond. Edinb. Dublin Philos. Mag. J. Sci. 34 (200) (1917) 94–98, https://doi.org/10.1080/14786440808635681.

[7] M.S. Plesset, A. Prosperetti, Bubble dynamics and cavitation, Annu. Rev. Fluid Mech. 9 (1) (1977) 145–185.

[8] J.B. Keller, M. Miksis, Bubble oscillations of large amplitude, J. Acoust. Soc. Am. 68 (2) (1980) 628–633.

[9] A. Prosperetti, A. Lezzi, Bubble dynamics in a compressible liquid. Part 1. First-order theory, J. Fluid Mech. 168 (1986) 457–478.

[10] I. Akhatov, O. Lindau, A. Topolnikov, R. Mettin, N. Vakhitova, W. Lauterborn, Collapse and rebound of a laser-induced cavitation bubble, Phys. Fluids 13 (10) (2001) 2805–2819.

[11] A. Zhang, S.-M. Li, P. Cui, S. Li, Y.-L. Liu, A unified theory for bubble dynamics, Phys. Fluids 35 (3) (2023).

[12] S. Nagrath, K. Jansen, R.T. Lahey Jr., I. Akhatov, Hydrodynamic simulation of air bubble implosion using a level set approach, J. Comput. Phys. 215 (1) (2006) 98–132.

[13] J. Huang, H. Zhang, Level set method for numerical simulation of a cavitation bubble, its growth, collapse and rebound near a rigid wall, Acta Mech. Sin. 23 (6) (2007) 645–653.

[14] E. Can, A. Prosperetti, A level set method for vapor bubble dynamics, J. Comput. Phys. 231 (4) (2012) 1533–1552.

[15] P.-W. Yu, S.L. Ceccio, G. Tryggvason, The collapse of a cavitation bubble in shear flows—a numerical study, Phys. Fluids 7 (11) (1995) 2608–2616.

[16] L. Liu, X. Yao, A. Zhang, Y. Chen, Numerical analysis of the jet stage of bubble near a solid wall using a front tracking method, Phys. Fluids 29 (1) (2017) 012105.

[17] S. Popinet, S. Zaleski, Bubble collapse near a solid boundary: a numerical study of the influence of viscosity, J. Fluid Mech. 464 (2002) 137–163.

[18] M. Koch, C. Lechner, F. Reuter, K. Köhler, R. Mettin, W. Lauterborn, Numerical modeling of laser generated cavitation bubbles with the finite volume and volume of fluid method, using openfoam, Comput. Fluids 126 (2016) 71–90.

[19] P. Koukouvinis, M. Gavaises, O. Supponen, M. Farhat, Simulation of bubble expansion and collapse in the vicinity of a free surface, Phys. Fluids 28 (5) (2016) 052103.

[20] Q. Zeng, S.R. Gonzalez-Avila, R. Dijkink, P. Koukouvinis, M. Gavaises, C.-D. Ohl, Wall shear stress from jetting cavitation bubbles, J. Fluid Mech. 846 (2018) 341–355.

[21] A. Tiwari, J.B. Freund, C. Pantano, A diffuse interface model with immiscibility preservation, J. Comput. Phys. 252 (2013) 290–309.

[22] K. Schmidmayer, F. Petitpas, S. Le Martelot, E. Daniel, ECOGEN: an open-source tool for multiphase, compressible, multiphysics flows, Comput. Phys. Commun. 251 (2020) 107093.

[23] S.H. Bryngelson, K. Schmidmayer, V. Coralic, J.C. Meng, K. Maeda, T. Colonius, MFC: an open-source high-order multi-component, multi-phase, and multi-scale compressible flow solver, Comput. Phys. Commun. 266 (2021) 107396.

[24] B.B. Taib, Boundary integral method applied to cavitation bubble dynamics, Ph.D. thesis, University of Wollongong, 1985.

[25] J. Blake, B. Taib, G. Doherty, Transient cavities near boundaries. Part 1. Rigid boundary, J. Fluid Mech. 170 (1986) 479–497.

[26] J. Blake, B. Taib, G. Doherty, Transient cavities near boundaries Part 2. Free surface, J. Fluid Mech. 181 (1987) 197–212.

[27] S. Zhang, J.H. Duncan, G.L. Chahine, The final stage of the collapse of a cavitation bubble near a rigid wall, J. Fluid Mech. 257 (1993) 147–181.

[28] O. Supponen, D. Obreschkow, M. Tinguely, P. Kobel, N. Dorsaz, M. Farhat, Scaling laws for jets of single cavitation bubbles, J. Fluid Mech. 802 (2016) 263–293.

[29] S. Li, Y. Saade, D. van der Meer, D. Lohse, Comparison of boundary integral and volume-of-fluid methods for compressible bubble dynamics, Int. J. Multiph. Flow 145 (2021) 103834.

[30] S. Li, A.-M. Zhang, R. Han, Counter-jet formation of an expanding bubble near a curved elastic boundary, Phys. Fluids 30 (12) (2018) 121703.

[31] A.A. Aganin, L. Kosolapova, V. Malakhov, Bubble dynamics near a locally curved region of a plane rigid wall, Phys. Fluids 34 (9) (2022) 097105.

[32] Q. Wang, K. Yeo, B. Khoo, K. Lam, Nonlinear interaction between gas bubble and free surface, Comput. Fluids 25 (7) (1996) 607–628.

[33] P. Robinson, J. Blake, T. Kodama, A. Shima, Y. Tomita, Interaction of cavitation bubbles with a free surface, J. Appl. Phys. 89 (12) (2001) 8225–8237.

[34] E. Klaseboer, B. Khoo, An oscillating bubble near an elastic material, J. Appl. Phys. 96 (10) (2004) 5808–5818.

[35] G. Curtiss, D. Leppinen, Q. Wang, J. Blake, Ultrasonic cavitation near a tissue layer, J. Fluid Mech. 730 (2013) 245–272.

[36] E. Klaseboer, B. Khoo, Boundary integral equations as applied to an oscillating bubble near a fluid-fluid interface, Comput. Mech. 33 (2004) 129–138.

[37] R. Han, A.-M. Zhang, S. Tan, S. Li, Interaction of cavitation bubbles with the interface of two immiscible fluids on multiple time scales, J. Fluid Mech. 932 (2022) A8.

[38] S. Wang, Q. Wang, D. Leppinen, A. Zhang, Y. Liu, Acoustic bubble dynamics in a microvessel surrounded by elastic material, Phys. Fluids 30 (1) (2018) 012104.

[39] T. Betcke, M. Scroggs, Bempp-cl: a fast Python based just-in-time compiling boundary element library, J. Open Sour. Softw. 6 (59) (2021) 2879.

[40] J. Dölz, H. Harbrecht, S. Kurz, M. Multerer, S. Schöps, F. Wolf, Bembel: the fast isogeometric boundary element C++ library for Laplace, Helmholtz, and electric wave equation, SoftwareX 11 (2020) 100476.

[41] A.F. Galvis, D.M. Prada, L.S. Moura, C. Zavaglia, J.M. Foster, P. Sollero, L.C. Wrobel, Besle: boundary element software for 3D linear elasticity, Comput. Phys. Commun. 265 (2021) 108009.

[42] A. Sieber, D. Preso, M. Farhat, Dynamics of cavitation bubbles near granular boundaries, J. Fluid Mech. 947 (2022) A39.

[43] A. Sieber, D. Preso, M. Farhat, Cavitation bubble dynamics and microjet atomization near tissue-mimicking materials, Phys. Fluids 35 (2) (2023) 027101.

[44] A.B. Sieber, D.B. Preso, M. Farhat, Ex uno plures: how to construct high-speed movies of collapsing cavitation bubbles from a single image, Exp. Fluids 64 (12) (2023) 187.

[45] C. Sanderson, R. Curtin, Armadillo: a template-based C++ library for linear algebra, J. Open Sour. Softw. 1 (2) (2016) 26.

[46] C. Sanderson, R. Curtin, A user-friendly hybrid sparse matrix class in C++, in: Mathematical Software–ICMS 2018: 6th International Conference, South Bend, IN, USA, July 24–27, 2018, in: Proceedings, vol. 6, Springer, 2018, pp. 422–430.

[47] M. Galassi, J. Davies, J. Theiler, B. Gough, G. Jungman, P. Alken, M. Booth, F. Rossi, R. Ulerich, GNU Scientific Library, Network Theory Limited, Godalming, 2002.

[48] L. Dagum, R. Menon, OpenMP: an industry standard API for shared-memory programming, IEEE Comput. Sci. Eng. 5 (1) (1998) 46–55.

[49] B. Schäling, The Boost C++ Libraries, Boris Schäling, 2011.

[50] C.R. Harris, K.J. Millman, S.J. van der Walt, R. Gommers, P. Virtanen, D. Cournapeau, E. Wieser, J. Taylor, S. Berg, N.J. Smith, R. Kern, M. Picus, S. Hoyer, M.H. van Kerkwijk, M. Brett, A. Haldane, J.F. del Río, M. Wiebe, P. Peterson, P. Gérard-Marchant, K. Sheppard, T. Reddy, W. Weckesser, H. Abbasi, C. Gohlke, T.E. Oliphant, Array programming with NumPy, Nature 585 (7825) (2020) 357–362.

[51] J.D. Hunter, Matplotlib: a 2D graphics environment, Comput. Sci. Eng. 9 (3) (2007) 90–95.

[52] W. Jakob, J. Rhinelander, D. Moldovan, pybind11 – seamless operability between C++11 and Python, https://github.com/pybind/pybind11, 2017.

[53] G.A. Curtiss, Non-linear, non-spherical bubble dynamics near a two fluid interface, Ph.D. thesis, University of Birmingham, 2009.

[54] C.E. Brennen, Cavitation and Bubble Dynamics, Cambridge University Press, 2014.

[55] C. Turangan, G. Ong, E. Klaseboer, B.C. Khoo, Experimental and numerical study of transient bubble-elastic membrane interaction, J. Appl. Phys. 100 (5) (2006) 054910.

[56] A. Pearson, Hydrodynamics of jet impact in a collapsing bubble, Ph.D. thesis, University of Birmingham, 2003.

[57] Q. Sun, E. Klaseboer, B.C. Khoo, D.Y. Chan, A robust and non-singular formulation of the boundary integral method for the potential problem, Eng. Anal. Bound. Elem. 43 (2014) 117–123.

[58] M. Walters, T. Phillips, A non-singular boundary element method for modelling bubble dynamics in viscoelastic fluids, J. Non-Newton. Fluid Mech. 235 (2016) 109–124.

[59] E. Klaseboer, K. Hung, C. Wang, C. Wang, B. Khoo, P. Boyce, S. Debono, H. Charlier, Experimental and numerical investigation of the dynamics of an underwater explosion bubble near a resilient/rigid structure, J. Fluid Mech. 537 (2005) 387–413.

[60] M.S. Longuet-Higgins, E. Cokelet, The deformation of steep surface waves on water – I. A numerical method of computation, Proc. R. Soc. Lond. Ser. A, Math. Phys. Sci. 350 (1660) (1976) 1–26.

[61] Q. Wang, Local energy of a bubble system and its loss due to acoustic radiation, J. Fluid Mech. 797 (2016) 201–230.

[62] T. Li, A. Zhang, S.-P. Wang, S. Li, W.-T. Liu, Bubble interactions and bursting behaviors near a free surface, Phys. Fluids 31 (4) (2019).

[63] J.R. Blake, D. Gibson, Growth and collapse of a vapour cavity near a free surface, J. Fluid Mech. 111 (1981) 123–140.